Available online at www.sciencedirect.com
ScienceDirect
Journal of Sound and Vibration 301 (2007) 458–480
JOURNAL OF SOUND AND VIBRATION
www.elsevier.com/locate/jsvi

Vibration analysis with lifting scheme and generalized cross validation in fault diagnosis of water hydraulic system

H.X. Chen, Patrick S.K. Chua, G.H. Lim*

School of Mechanical and Aerospace Engineering, Nanyang Technological University, 50 Nanyang Avenue, Singapore 639798, Singapore

Received 19 August 2005; received in revised form 6 July 2006; accepted 3 August 2006
Available online 22 November 2006

Abstract

This paper presents a novel method to analyze the vibration signals in the fault diagnosis of water hydraulic motor. The method of feature extraction from the vibration signals of the water hydraulic motor based on the second-generation wavelet is investigated. The second-generation wavelet consists of a lifting scheme. The algorithm and method of multi-decomposition based on the lifting scheme for vibration analysis is developed. The denoise method for the vibration signals is proposed on the lifting scheme and the generalized cross validation (GCV). The relationship between the signal-to-noise (SNR) and GCV is presented. The corrupted simulated signal is used to test the proposed denoise algorithm. The method for extracting the feature values from the impulse vibration signals based on the statistical method is studied. The results show the applicability of this method for fault diagnosis of a water hydraulic motor.
© 2006 Elsevier Ltd. All rights reserved.

1. Introduction

With the increasing environmental impact of operating oil-based hydraulic system and the concern raised by environmentally conscious organizations, a most exciting area of development in the fluid power industry over the past few years has been in water hydraulics, which involves using tap water as a viable alternative to oil in fluid power transmission. Water hydraulic systems have been used in the farming, forestry, food, pharmaceutical and paper industries [1–3].

The axial piston motor is commonly applied to provide high torque and performance for water hydraulic system. Pistons are the principal operating elements of reciprocating machines and their fundamental performance invariably depends on the smooth and efficient motion of pistons in the cylinder bore. The axial piston swash-plate-type hydraulic motor comprises a discrete number of pistons that reciprocate in a sinusoidal fashion for the purpose of torque output. The basic force within axial piston pump has been analyzed and summarized. The instantaneous torque exerted on the shaft has been computed and the resonant frequencies of the pump that occur at even-multiples of the ''piston-pass'' frequency have been shown [4]. The mathematical equations describing swash-plate behavior have been derived from the general hydraulic and mechanical considerations [5].

*Corresponding author. Fax: +65 6791 1859.
E-mail address: mghlim@ntu.edu.sg (G.H. Lim).

0022-460X/$ - see front matter © 2006 Elsevier Ltd. All rights reserved.
doi:10.1016/j.jsv.2006.08.041

The dynamic behavior of the axial piston motor is nonlinear and the factors that influence the performance of the axial piston motor are complicated. Theoretical analysis of the vibration sources and transmission paths of the water hydraulic axial piston motor has not attracted as much attention as experimental investigations, due to the complexity in modeling. However, some recent works have been reported. The vibration energy transmission characteristics from the cylinder to a swash-plate within an axial piston pump had been studied by Qiu et al. [6]. Qi and Lu [7] investigated the vibration and condition monitoring problems of oil hydraulic axial piston pumps. Investigations showed that the main source of vibration is the impact between the slipper and swash plate when the piston/slipper moved into a pre-compression process. This impact force may excite a resonant vibration of the pump housing. Bahr et al. [8] developed a mathematical model to investigate the vibration characteristics of the pumping mechanism of oil hydraulic constant-power axial piston pumps with conical cylinder blocks. They applied Fourier transform in the vibration analysis of the axial piston pump. But Fourier analysis has some inherent limitations in the analysis of the non-stationary signal. It cannot characterize the impulsive vibration signal in the reciprocating or rotating machine.

The wavelet theory [9] has become one of the emerging and fast-evolving mathematical and signal-processing tools due to its many distinct merits. It can perform maps with good time resolution at high frequency to identify the impulse vibration signal at which transient phenomena takes place. Serkhar [10] detected the crack through wavelet transform for a run-up rotor by continuous wavelet transform (CWT). Wavelet analysis is applied to analyze the pressure signal for health diagnosis of the pump [11]. The vibration signal in the rotating and reciprocating machinery is non-stationary in nature. The vibration signals produced by industrial machinery are vital indicators of machinery health [12–16].

In this paper, a novel approach is proposed for using vibration analysis for the fault diagnosis of the water hydraulic motor. The proposed method is based on second-generation wavelets that are constructed by a lifting scheme. A lifting scheme is a new method for constructing wavelets. It gradually constructs a new wavelet with improved properties. The classical wavelets are known as translation and dilation of one fixed function, where the Fourier transform is very important. The second-generation wavelet with lifting scheme is entirely spatial and needs less computational time compared with CWT.

The organization of this paper is as follows. Section 2 describes the vibration mechanism and characteristics. Section 3 discusses the second-generation wavelet to analyze the signal. Section 4 analyzes generalized cross validation (GCV) for the signal de-noising to improve the signal-to-noise ratio (SNR). Section 5 describes the experimental rig and apparatus of hydraulic motor and water hydraulic system. In Section 6, the multi-decomposition based on the lifting scheme and GCV is proposed. The simulated signal and experimental vibration signal are analyzed by the proposed method for the fault detection of piston crack in a water hydraulic motor. Section 7 concludes the paper.

2. Water hydraulic motor vibration mechanism

The actuator studied here is a five-piston axial piston motor used in a water hydraulic system. An accelerometer mounted on the casing of the MAH 12.5 water hydraulic motor was used to obtain the vibration signal from the motor. The complete water hydraulic system was provided by Danfoss Inc. and Fig. 1 shows the general structure of the water hydraulic motor [17]. An axial piston motor consists mainly of a valve port plate with inlet and outlet ports, a swash-plate, an outer shell, a cylinder block, pistons with shoes, a bias spring, a port flange and a shaft. The piston fits within the bores of the cylinder barrel and is on the same axis as the output shaft. The swash-plate is positioned at an angle and acts as a surface on which the piston shoes travel. The shoes are held in contact with the swash-plate by the retaining rings and the bias spring. The port plate separates the incoming fluid from the discharging fluid. The output shaft is connected to the cylinder barrel.

The hydrostatic axial piston motor is driven by the pistons within the cylindrical block. The pistons are nested in a circular array in the cylinder at equal intervals about the z-axis. The cylinder block is held tightly against the valve cover using the compressed force of the springs. The valve cover is separated from the cylinder block by a thin film, which forms a hydrodynamic bearing between them under normal operating conditions. A ball-and-socket joint connects the base of each piston to a slipper. The slippers themselves are

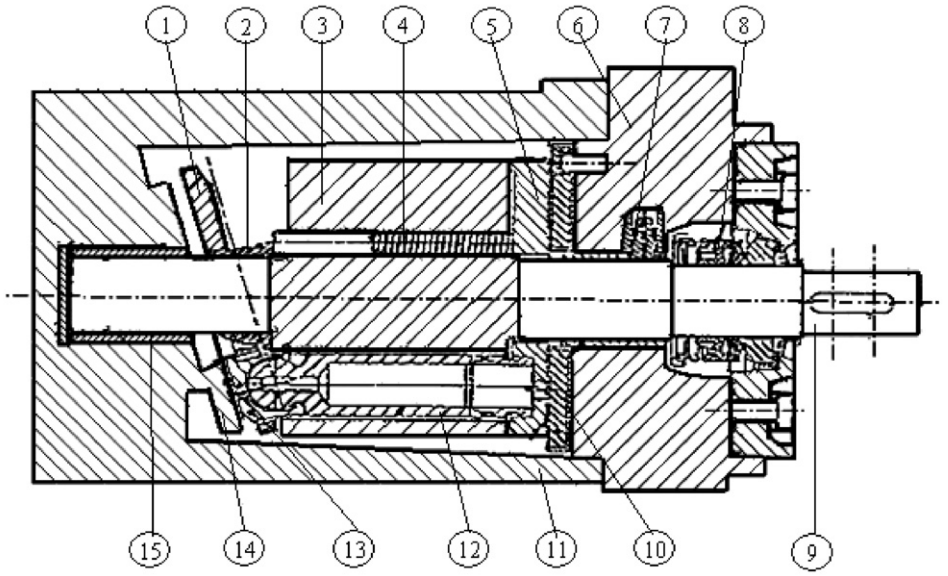

1. retaining ring
2. bushing with spherical outer surface
3. cylinder block
4. spring
5. thrust plate
6. port flange
7. hydrostatic bearings
8. shaft seal
9. motor shaft
10. valve port plate
11. outer shell
12. piston
13. shoe
14. swash plate
15. bearing

Fig. 1. Swash plate water hydraulic motor with five pistons.

kept in reasonable contact with the swash plate support by the retaining rings. The hydrostatic and hydrodynamic bearing surface separates the slippers from the swash plate support.

The pistons drive the cylinder block to rotate around the z-axis at a constant angular speed by the pressure in the supply port. Each piston periodically passes over the supply and return line ports on the valve plate. The slippers are held against the inclined plane of the swash plate. The pistons undergo an oscillatory displacement in and out of the cylinder block. When the piston passes over the supply port, the pressure causes the piston to withdraw from the cylinder block. The piston passes over the return line port and the fluid is pushed out of the piston chamber. These motions of the piston and cylinder block repeat and the basic task of the output torque is then completed.

As the water enters the inlet and exits at the outlet of the hydraulic motor, the pressure in the cylinder chamber alternates from high pressure to low pressure. This causes pressure pulsation to occur. The total cylinder area inside a supply port is variable as a result of the cyclic variations of the piston passing through the supply port. It generates the variations of the axial output moment. The variations of the forces are applied from the piston to the swash plate and the valve cover. The force between the support for the swash plate and the valve cover is opposite in direction. The hydraulic motor body vibrates as a result.

A hydraulic system generates more complicated vibration (noise) on account of the interaction between the two pressure pulsations produced by the motor and pump. The fluid-borne vibration causes the structure-borne vibration that has a negative effect on the life span of motor and pump. Kojima and Shinada [18] and Edge and Johnston [19] investigated the fluid-borne vibration in a combination circuit consisting of a pump, a motor and a connecting pipe. The pressure ripple is characteristic of a fundamental component at piston frequency obtained in a general hydraulic system. The pressure ripples in piston pumps and motor are mostly due to an intermittent impulsive back flow into the cylinder chamber in the neighborhood of the bottom and top dead center. The characteristic frequencies of fluid-borne vibration in hydraulic system have two flow and

pressure pulsating sources that the pump and motor generate, respectively. The fundamental frequencies of water hydraulic motor and pump are determined as follows:

$$f = zN, \tag{1}$$

where f is the fundamental frequency of the hydraulic pump and motor, z is the piston number, and N is the angular speed. In this work, fundamental frequency f was 52.5 Hz, piston number z was 5 and rotational speed N was 630 rev/min.

3. Second-generation wavelet

3.1. Wavelet subband transform

The wavelet analysis produces a family of hierarchically organized decompositions. The level is chosen based on a desired low-pass cutoff frequency. The one-dimensional wavelet decomposition represents a real-value discrete-time signal in terms of shifts and dilations of a low-pass scaling function and a bandpass wavelet function. The wavelet decomposition consists of a set of scaling coefficients (A) that represent the coarse signal information and wavelet coefficients (D).

Fig. 2 shows the general block scheme of wavelet subband transform [20]. The low-pass filter $\tilde{h}$ and band pass filter $\tilde{g}$ are used for the forward transform followed by subsampling. The low-pass synthesis filter h and high-pass synthesis filter g are used for the inverse transform after the upsamples. The four filters h, g, $\tilde{h}$, and $\tilde{g}$, of WT are finite impulse response (FIR) filters. The condition for the perfect reconstruction is given as

$$\tilde{h}(z^{-1})h(z) + \tilde{g}(z^{-1})g(z) = 2, \tag{2}$$

$$\tilde{h}(-z^{-1})h(z) + \tilde{g}(-z^{-1})g(z) = 0. \tag{3}$$

The above shows that half of the filtered samples are thrown away which is not efficient. In order to solve this problem, the signal would be subsampled before the filtering. The input signal X as shown in Fig. 2 is divided as even samples (x_e) and odd samples (x_o). The scale coefficients and wavelet coefficients can be obtained in the polyphase representation

$$\begin{pmatrix} D(z) \\ A(z) \end{pmatrix} = \begin{pmatrix} \tilde{h}_e(z) & \tilde{h}_o(z) \\ \tilde{g}_e(z) & \tilde{g}_o(z) \end{pmatrix} \begin{pmatrix} x_e(z) \\ z^{-1}x_o(z) \end{pmatrix}. \tag{4}$$

The polyphase matrix is defined as

$$\tilde{P}(z) = \begin{pmatrix} \tilde{h}_e(z) & \tilde{h}_o(z) \\ \tilde{g}_e(z) & \tilde{g}_o(z) \end{pmatrix}. \tag{5}$$

The even output sample (y_e) and odd output sample (y_o) from the inverse wavelet transform in Fig. 2 is given in the polyphase matrix

$$\begin{pmatrix} y_e(z) \\ z.y_o(z) \end{pmatrix} = \begin{pmatrix} h_e(z) & g_e(z) \\ h_o(z) & g_o(z) \end{pmatrix} \begin{pmatrix} D_e(z) \\ A_e(z) \end{pmatrix}. \tag{6}$$

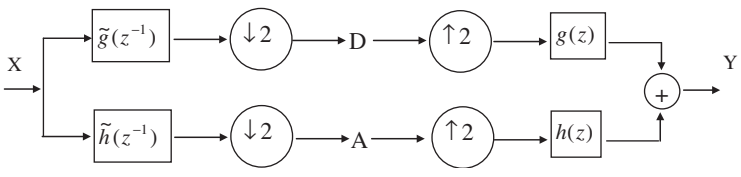

Fig. 2. The block scheme of subband transform.

The second polyphase matrix is defined as

$$P(z) = \begin{pmatrix} h_e(z) & g_e(z) \\ h_o(z) & g_o(z) \end{pmatrix}. \tag{7}$$

Fig. 3 shows the one-stage filter for signal decomposition and reconstruction using polyphase matrices. Eqs. (4) and (6) are incorporated in split and merge boxes. For the perfect reconstruction, the following equation can be obtained:

$$\tilde{P}(z^{-1})P(z) = 1. \tag{8}$$

The following equation can be derived from Eq. (8) and Cramer's rule:

$$\begin{aligned} \tilde{h}_e(z) &= g_o(z^{-1}), \quad & \tilde{h}_o(z) &= -g_e(z^{-1}), \\ \tilde{g}_e(z) &= -h_o(z^{-1}), \quad & \tilde{g}_o(z) &= h_e(z^{-1}). \end{aligned} \tag{9}$$

Eq. (9) implies the following equation as

$$\tilde{h}(z) = -z^{-1}g(-z^{-1}), \quad \tilde{g}(z) = z^{-1}h(-z^{-1}). \tag{10}$$

3.2. Lifting scheme

Wavelet represents the general functions as data building blocks, which can obtain the important data sets with a small number of coefficients. The second-generation wavelet transform is constructed by the lifting scheme. The lifting scheme is a spatial or time-domain construction of biorthogonal wavelets [20,21]. The basic idea behind lifting is that it provides a simple relationship between all multi-resolution analyses that share the same low-pass filter or high-pass filter. The low-pass filter gives the coefficients of the refinement relation, which entirely determines the scaling functions where the coefficients are given by the high-pass filter.

The lifting scheme consists of iterations of the following three basic operations as shown in Fig. 4. Firstly, the split divides the original data into two subsets. The original signal is split to the even indexed points and the odd indexed points, that is $x_e[n] = x[2n]$ and $x_o[n] = x[2n+1]$. This generates the wavelet coefficients $d[n]$ as the error by the predicting operator P:

$$d[n] = x_o[n] - P(x_e[n]). \tag{11}$$

The process of computing a prediction and recording it is called a lifting step. The original signal is transformed from (x_o, x_e) to (x_o, d). There is aliasing in the even samples due to the subsample. The second lifting step is introduced to solve the problem. The update combines $x_e[n]$ and $d[n]$ to obtain the scaling

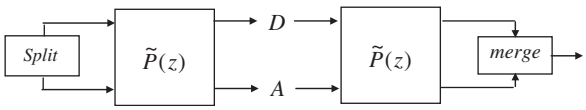

Fig. 3. The polyphase representation for signal analysis and reconstruction.

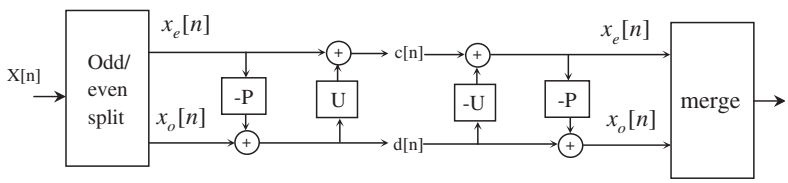

Fig. 4. Lifting step and inverse lifting step.

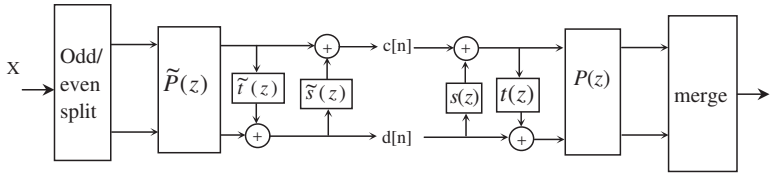

Fig. 5. Low-pass subband is lifted with help of high-pass subband (predict) and high-pass subband is lifted with help of low-pass subband (update).

coefficients $c[n]$ that represents the coarse approximation in the original signal. The updated operator U is used with the wavelet coefficients for $x_e[n]$.

$$c[n] = x_e[n] + U(d[n]). \tag{12}$$

These three steps form the lifting stage. The iterations of the lifting stage on the output samples create the complete set of discrete wavelet transform scaling and wavelet coefficients $c^j[n]$ and $d^j[n]$ at each scale j.

Fig. 5 shows that the low-pass subband is lifted with the help of the high-pass subband (predict) and the high-pass subband is lifted with the help of the low-pass subband (update). The lifting steps are easily inverted. The following equations for invertible lifting are derived:

$$x_e[n] = c[n] - U(d[n]), \quad x_o[n] = d[n] + P(x_e[n]). \tag{13}$$

The lifting theory shows that any other new finite filter g^l complementary to h is of the form that is called the update step.

$$g^l(z) = g(z) + h(z)s(z^2), \tag{14}$$

where $s(z^2)$ is a Laurent polynomial. The new polyphase matrix is shown as

$$P^l(z) = \begin{pmatrix} h_e(z) & h_e(z)s(z) + g_e(z) \\ h_o(z) & h_o(z)s(z) + g_o(z) \end{pmatrix} = P(z)\begin{pmatrix} 1 & s(z) \\ 0 & 1 \end{pmatrix}. \tag{15}$$

The new filter $\tilde{h}^{\text{new}}(z)$ complementary to $\tilde{g}(z)$ is indicated as

$$\tilde{h}^l(z) = \tilde{h}(z) + \tilde{g}(z)\tilde{s}(z^2). \tag{16}$$

The new dual polyphase matrix is given by

$$\tilde{P}^l(z) = \begin{pmatrix} \tilde{h}_e(z) + \tilde{g}_e(z)\tilde{s}(z) & \tilde{h}_o(z) + \tilde{g}_o(z)\tilde{s}(z) \\ \tilde{g}_e(z) & \tilde{g}_o(z) \end{pmatrix} = \begin{pmatrix} 1 & \tilde{s}(z) \\ 0 & 1 \end{pmatrix}\tilde{P}(z). \tag{17}$$

Similarly, the high-pass subband is lifted with the help of the low-pass subband. The dual lifting equations (the predict step) are given as

$$h^l(z) = h(z) + g(z)t(z^2), \tag{18}$$

$$P^l(z) = \begin{pmatrix} h_e(z) + g_e(z)t(z) & g_e(z) \\ h_o(z) + g_o(z)t(z) & g_o(z) \end{pmatrix} = P(z)\begin{pmatrix} 1 & 0 \\ t(z) & 1 \end{pmatrix}, \tag{19}$$

$$\tilde{g}^l(z) = \tilde{g}(z) + \tilde{h}(z)\tilde{t}(z^2), \tag{20}$$

$$\tilde{P}^l(z) = \begin{pmatrix} \tilde{h}_e(z) & \tilde{h}_o(z) \\ \tilde{g}_e(z) + \tilde{h}_e(z)\tilde{t}(z) & \tilde{g}_o(z) + \tilde{h}_o(z)\tilde{t}(z) \end{pmatrix}. \tag{21}$$

Some wavelet filters such as Haar, Daubechies, and Cubic B-splines wavelet function can be used to build the second-generation wavelet transform into lifting steps. Haar wavelet is used in this research to generate the

lifting step. Haar wavelet has the following filters:

$$h(z) = 1 + z^{-1}, \quad g(z) = -1/2 + 1/2z^{-1},$$
$$\tilde{h}(z) = 1/2 + 1/2z^{-1}, \quad \tilde{g}(z) = -1 + 1z^{-1}. \tag{22}$$

The multi-decomposition consists of the following implementation:

$$s_l^{(0)} = x_{2l}, \quad d_l^{(0)} = x_{2l+1},$$
$$d_l = d_l^{(0)} - s_l^{(0)}, \quad s_l = s_l^{(0)} + 1/2d_l. \tag{23}$$

4. Generalized cross validation

The following model of a discrete noisy signal is considered:

$$y = f + \varepsilon. \tag{24}$$

The vector y represents the input signal and f is an unknown and deterministic signal. The noise ε is stochastic signal. The wavelet representation is used to reconstruct the original data. The following transform is considered:

$$\upsilon = Wf, \quad \zeta = W\varepsilon, \quad w = Wy = \upsilon + \zeta. \tag{25}$$

This transform localizes the most important spatial and frequency characteristics of a regular signal in a limited number of wavelet coefficients. The Donoho's 'soft-thresholding' or 'shrinking' function is proposed to reduce the small coefficients.

The shrinking (soft-thresholding) operations can be represented as

$$w_\delta = D_\delta w, \tag{26}$$

where $D_\delta = \mathrm{diag}[d_{ii}]$ with

$$d_{ii} = \begin{cases} 0 & \text{if } |w_i| < \delta, \\ 1 - \delta/|w_i| & \text{otherwise} \end{cases}$$

and δ is the optimal soft-threshold value. The elements of the matrix D_δ depend on the signal w. In the same way, the inverse transform can be obtained

$$y_\delta = A_\delta y, \tag{27}$$

where A_δ is the influence matrix $A_\delta = W^{-1}D_\delta W$.

The optimal parameter δ is applied to the wavelet coefficients to improve the maximum SNR. It means to minimize the mean square error $R(\delta) = (1/N)||\omega_\delta||^2 = (1/N)||w_\delta - \upsilon||^2 = (1/N)||W\varepsilon_\delta||^2$. However, the signal f is unknown. The optimal threshold cannot be found. Donoho and Johnstone [22] proposed to use the 'universal threshold' estimation

$$\delta = \sqrt{2\,\log(N)}\sigma. \tag{28}$$

This equation needs the knowledge of the noise variance, which is not readily available in practice.

In order to find the optimal threshold directly by using the input data, Weyrich and Warhola [23] applied the idea of cross validation to obtain the excellent results. This cross validation [24] is a function of the threshold value only based on the input data. Its minimum is a good approximation for the optimal threshold.

In order to minimize the function $R(\delta)$, a new matrix is introduced as

$$D'_{ij} = \frac{\partial w_{\delta i}}{\partial w_j}. \tag{29}$$

Here if $i \neq j$, then $D'_{ij} = 0$. For $i = j$, the following equation can be defined:

$$D'_{ii} = \begin{cases} 0 & \text{if} \quad |\mathrm{w_i}| < \delta, \\ 1 & \text{otherwise.} \end{cases} \tag{30}$$

The trace of the matrix D' is calculated as

$$\mathrm{Tr}(D') = \#\{i | w_{\delta i} \neq 0\}. \tag{31}$$

The derivative influence matrix is introduced and defined as

$$A' = W^{-1} D' W \quad \text{and} \quad \mathrm{Tr}(A') = \mathrm{Tr}(D'). \tag{32}$$

The cross validation in an informal way is introduced to minimize the error function based on an unknown exact signal. The GCV is defined as

$$\mathrm{GCV}(\delta) = V(\delta) = \frac{(1/N)||y - y_\delta||^2}{[\mathrm{Tr}(I - A')/N]^2}. \tag{33}$$

The parameter GCV is the estimation of the optimal threshold δ.

5. Experimental setup and procedure

The water hydraulic motor test apparatus as shown in Fig. 6 consists of a MAH12.5 Nessie water hydraulic motor, a brushless servo motor, a digital torque meter and a water hydraulic system. The water hydraulic system allows axial piston motor operation in the range of 300–3000 rev/min and 0–6 N m. The digital torque meter is made up of a detector and an operational display. The detector converts the shaft-rotating angle, which is proportional to an applied axis torque of the motor into a phase difference signal. In order to measure the rotational speed of the detector shaft, the detector is provided with a rotation detector and a gearbox on the torsion bar. The transmission ratio of the gearbox is 3.4. The torque converter processes the signals and shows the results as the digital value of torques and rotational speeds. The brushless servo motor is superior in providing the precise and stable torque in the range of 0–10.2 N m for the motor. The servo digital control modules were used to control the brushless servo motor and cause it to generate the constant output torque. The range of the output torque by servo motor is 3.0 N m. The arbitrary function generator can output DC voltage to the servo digital control modules for adjusting the output torque of the servo control motor. The servo digital control system can also be controlled and displayed by the interface control software installed in a personal computer.

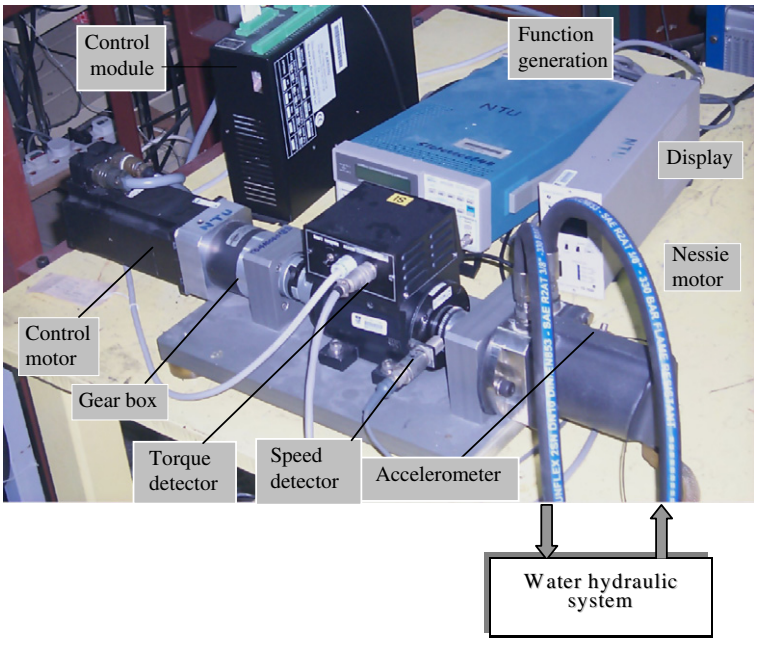

Fig. 6. Water hydraulic motor test system.

Fig. 7. Piston cracks in back section and front section.

A piezoelectric accelerometer (*Brüel & Kjaer* type 4393) was mounted on the shell of the motor near the inlet of the water hydraulic motor. The output signal from this accelerometer was simultaneously fed to the amplifier and 5B41 filters for noise reduction and anti-aliasing. A data acquisition card (AT-MIO-16L-9 from National Instruments Inc.) that was controlled by LabView was used to convert analog signals to digital signals. The sampling rate obeys the Nyquist formula and was chosen to be 2 kHz that was sufficient for the type of signals considered in this work. A time record of 2000 data points was taken in each experimental run. The rotational speed of the motor was 630 rev/min. The output axis torque of Nessie motor was 5 N m. The data points of vibration signal covered one rotational period of the motor detected by the torque and speed detector. The signal characteristic can be fully described within the rotational period.

Piston crack was simulated in the axial piston of the Nessie motor by using an electro-discharge machine. The introduced crack is 0.1 mm wide. There were five operational conditions in this research work. They were normal condition (NC) and four faulty conditions with four different kinds of piston cracks. For the Nessie motor, in order to detect the different piston crack locations as shown in Fig. 7 and piston crack lengths, four kinds of piston cracks were introduced as follows:

(1) *Back long crack* (*BLC*): The crack is 10 mm long and located in the back section of the piston.
(2) *Back short crack* (*BSC*): The crack is 5 mm long and located in back section of the piston.
(3) *Front long crack* (*FLC*): The crack is 10 mm long and located in the front section of the piston.
(4) *Front short crack* (*FSC*): The crack is 5 mm long and located in the front section of the piston.

6. Results and discussion

6.1. Noise reduction of vibration signal

Wavelet denoising is a noise reduction method by transforming the corrupted signals into the wavelet domain by applying thresholding in the wavelet domain and inversely transforming the denoised wavelet coefficients. The wavelet coefficients can be obtained by the decomposition of Haar wavelet filter into the lifting step. The discrete wavelet transform based on the lifting step is used for the multi-level wavelet decomposition. At each scale, GCV is used as the threshold to process and discriminate the original signals and noise.

The procedure to be executed can be described as follows:

(1) Obtain the wavelet coefficient by computing $w = Wy$, using the multi-level decomposition based on the second-generation wavelet, that is lifting scheme.
(2) Determine a start threshold value.

(3) Minimize the value of the parameter GCV(δ).
(4) Compute $w_\delta = D_\delta w$.
(5) Inverse wavelet transform: $y_\delta = W^{-1} w_\delta$ to obtain the denoised signal.

The simulated signals were generated by the following functions to test this proposed algorithm. Figs. 8(a) and (b) show the original signals and the corrupted signals with SNR of 1 dB. Figs. 8(c)–(e) show the de-noise signals by the multi-decomposition at first scale, second scale and third scale, respectively. The SNR is improved at second scale and third scale compared with at first scale.

$$y_1 = 0.01\ \sin(120\pi t) + 0.003\ \sin(240\pi t) + 0.02\ \cos(400\pi t). \tag{34}$$

Fig. 9 shows the relation between the SNR and GCV at the different scales. In Fig. 9(a), the corrupted signal is denoised at the first scale. The SNR increases with the decrease of the GCV. The SNR is improved by up to about 9 dB. The range of GCV is between 6×10^{-4} and 4×10^{-4}. Fig. 9(b) shows the results at second scale of the multi-decomposition. The SNR increases from 9.7 to 14.7 dB. The GCV value decreases from 1.6×10^{-3} to 0.8×10^{-3}. The SNR value increases with the decrease of the GCV value. Fig. 9(c) shows the similar results at third scale as that at first and second scale. The SNR is up to 19.5 dB.

6.2. Statistical feature extraction of localized impulse vibration signal

The wavelet transform can be used to represent efficiently the localized features of the signals. It is an ideal tool for the extraction of features, especially if the vibration is induced by the fluid, which creates vibration that is characteristic of the impulse signal. The impulse component in the vibration signals is an important feature to diagnose the mechanical condition. As shown in Fig. 10, the original signal is decomposed into the scaling coefficients $c_1[n]$ and wavelet coefficients $d_1[n]$. The multi-decomposition based on the lifting scheme splits the scaling coefficients into two parts using the same scheme, producing $c_2[n]$ and $d_2[n]$ in the next step. Hence, the wavelet decomposition of the signal at scale j has the structure $[c_j[n], d_j[n], \ldots, d_j[n]]$. The terminal nodes of wavelet decomposition tree are shown in Fig. 10. In this work, the number of the decomposition level was selected to be 3. As shown in Fig. 9, it was enough and effective for GCV to denoise the experimental vibration signal and improve the SNR within the three-level decompositions. The other key point was to extract feature values from the wavelet coefficients in the decomposition of the impulse vibration signal, which was more effective in the three-level decompositions.

Fig. 11 shows the typical wavelet multi-decomposition of the experimental vibration signal. Fig. 11(a) shows the original signal. Fig. 11(b) shows the scaling coefficient at first scale ($c_1[n]$). Fig. 11(c) shows the wavelet coefficient $d_1[n]$ that is characteristic of the impulse signal. The impulse signal is produced by the pumping mechanism when the piston rotates from the return line to supply line, which results in the overshoot of the piston pressure. Figs. 11(d) and (e) show the scaling coefficients $c_2[n]$ and wavelet coefficients $d_2[n]$ at second scale.

The scaling coefficients in the multi-decomposition of the vibration signal are the important information in the impulse vibration signals. In order to diagnose the different conditions, the wavelet scaling coefficients at first scale are used to extract the features.

The vibration signal is characteristic of impulse vibration, which is generated by the fluids. The intermittency index is an effective feature to display the impulse energy in the vibration signal in the fluid power system [25]. The intermittency index is used to the wavelet scaling coefficients at first scale. The intermittency at each scale can be viewed directly using the intermittency index defined as

$$I_{m,n} = \frac{(T_{m,n})^2}{\left\langle T_{m,n}^2 \right\rangle_m} \quad \left\langle T_{m,n}^2 \right\rangle_m = \sum\nolimits_{n=1}^{2^{11-m}} T_{m,n}^2 \Big/ 2^{11-m}, \quad m = 1, 2, 3. \tag{35}$$

Here $T_{m,n}$ are the wavelet coefficients at scale index m. $\left\langle T_{m,n}^2 \right\rangle_m$ is the second-order statistical moment of the wavelet coefficients at scale index m. For example, a constant value of $I_{m,n} = 1$ for all m and n means that there is no flow intermittency. A value of 10 at a specific set of indices m and n means that there is 10 times more

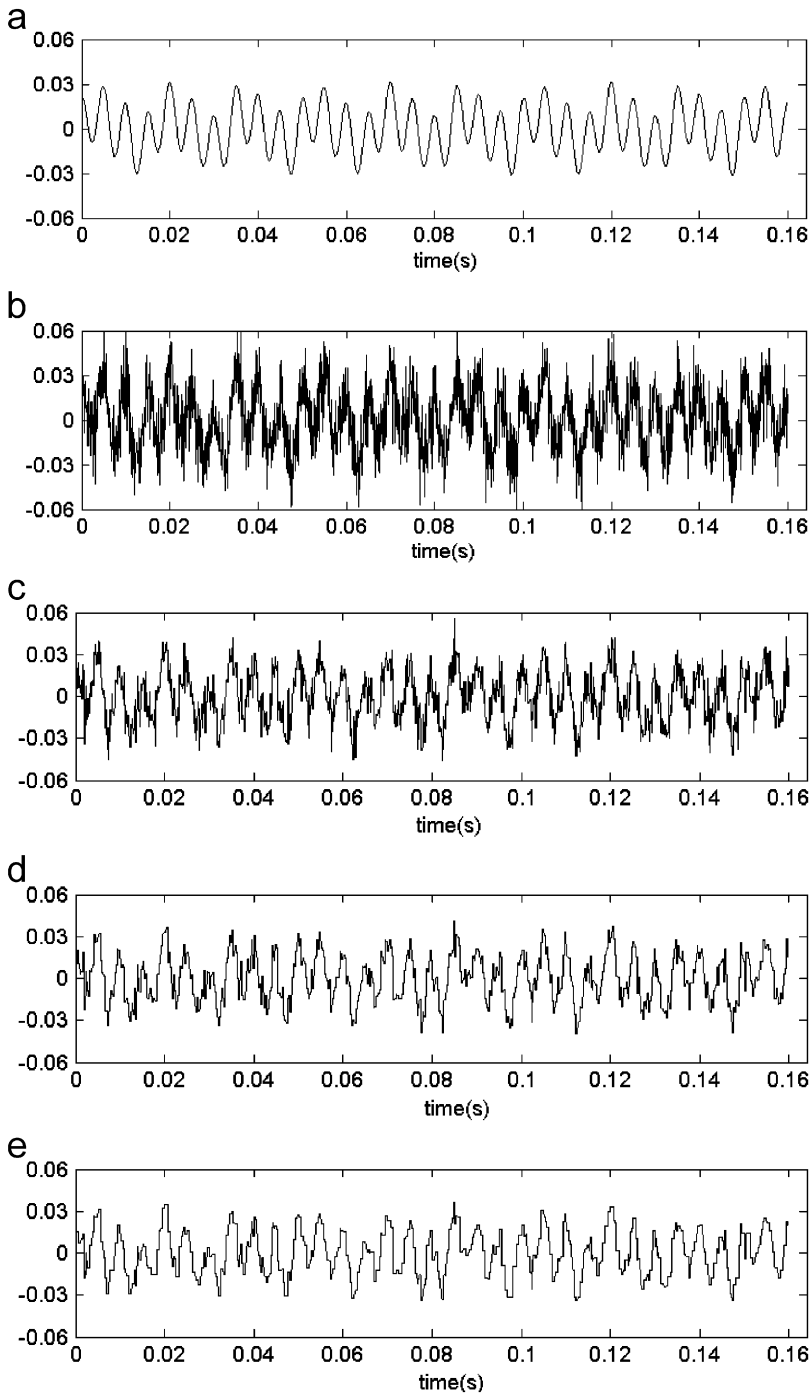

Fig. 8. Original signal, corrupted signal and denoised signal by different scale decomposition with GCV: (a) original signal, (b) corrupted signal with SNR of 1 dB, (c) clean signal by first scale, (d) clean signal by second scale and (e) clean signal by third scale.

energy contained within the coefficients at that location than for the temporal mean at that scale at that location in the signal. Fig. 12 shows the intermittency indices at the first wavelet scale for the vibration signals under the five conditions. There are different amplitudes and number in the intermittency indices.

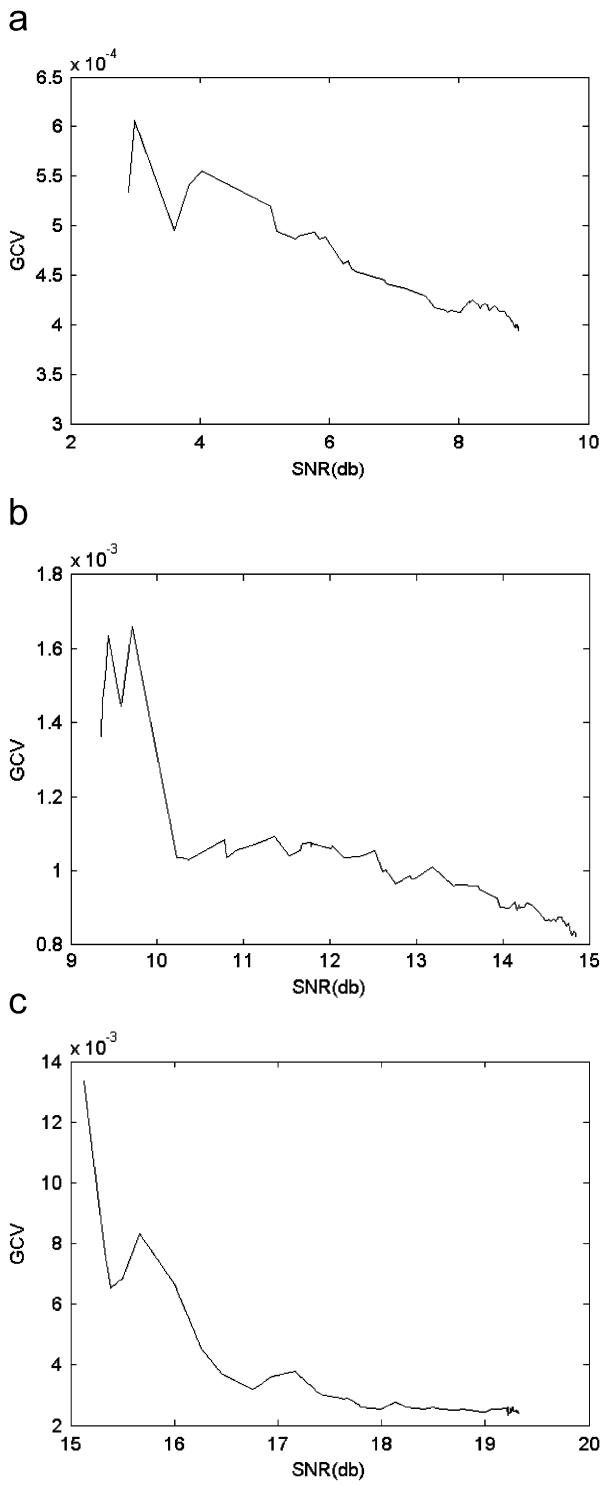

Fig. 9. The relation between SNR and GCV at the different scale: (a) first scale, (b) second scale and (c) third scale.

Fig. 13 shows the statistical probability distribution (SPD) of the mean of the highest intermittency indices at the first wavelet scale. The results show the different probability distribution under five different conditions. Fig. 13(a) shows the mean of SPD was about 28 and the range of SPD was between −4 and 60 under BLC

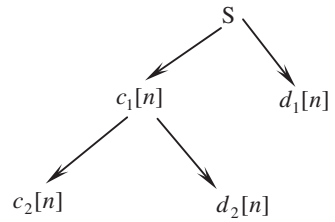

Fig. 10. Wavelet decomposition tree based on lifting scheme.

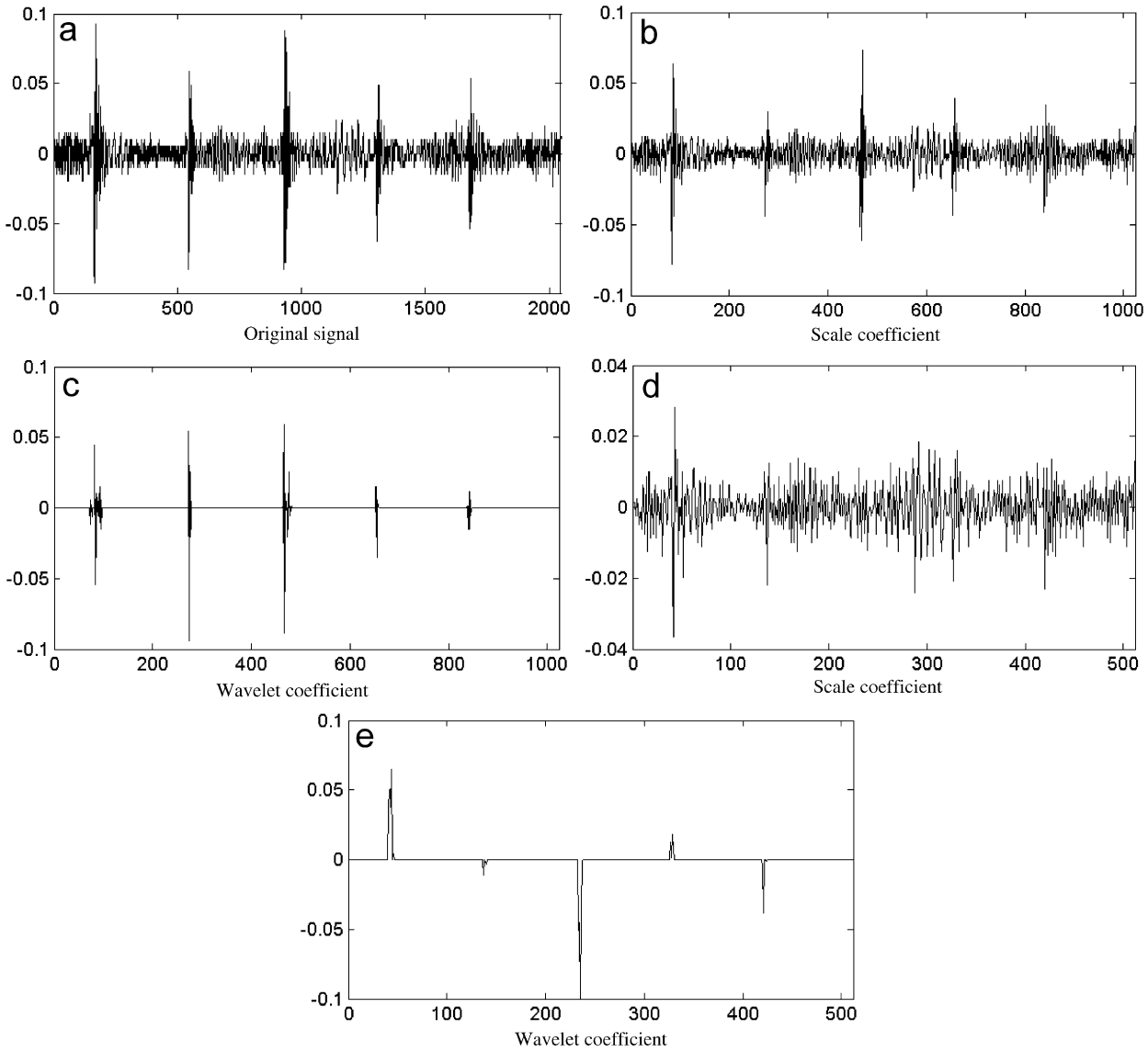

Fig. 11. The multi-decomposition based on the lifting scheme of the experimental vibration signal.

condition. Fig. 13(b) shows the mean of SPD was about 14 and the range of SPD was between 0 and 28, which was different from the results under BLC condition. In Fig. 13(c), the mean of SPD was 41.5 and the range of SPD was between 3 and 80 under FLC condition, which was more than that under BLC and BSC conditions.

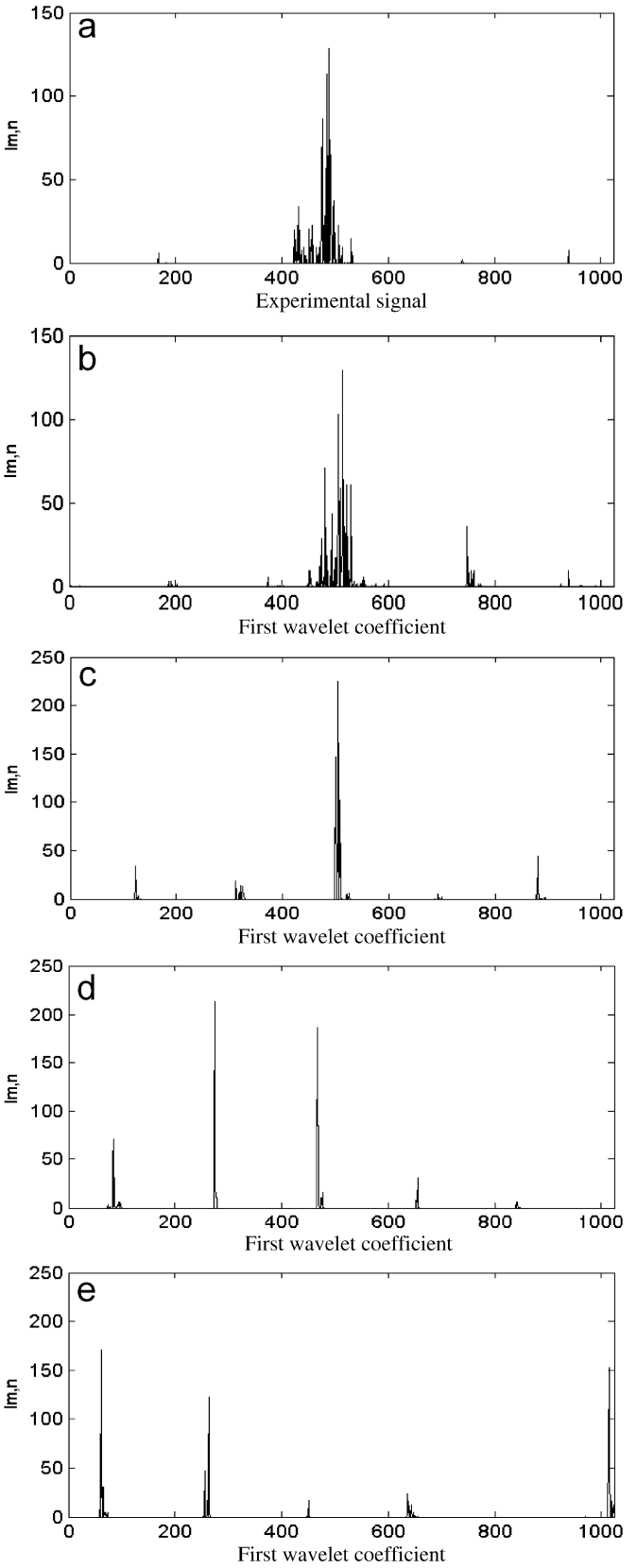

Fig. 12. Intermittency indices at the first wavelet scale for the vibration signal under five conditions: (a) BLC, (b) BSC, (c) FLC, (d) FSC and (e) NC.

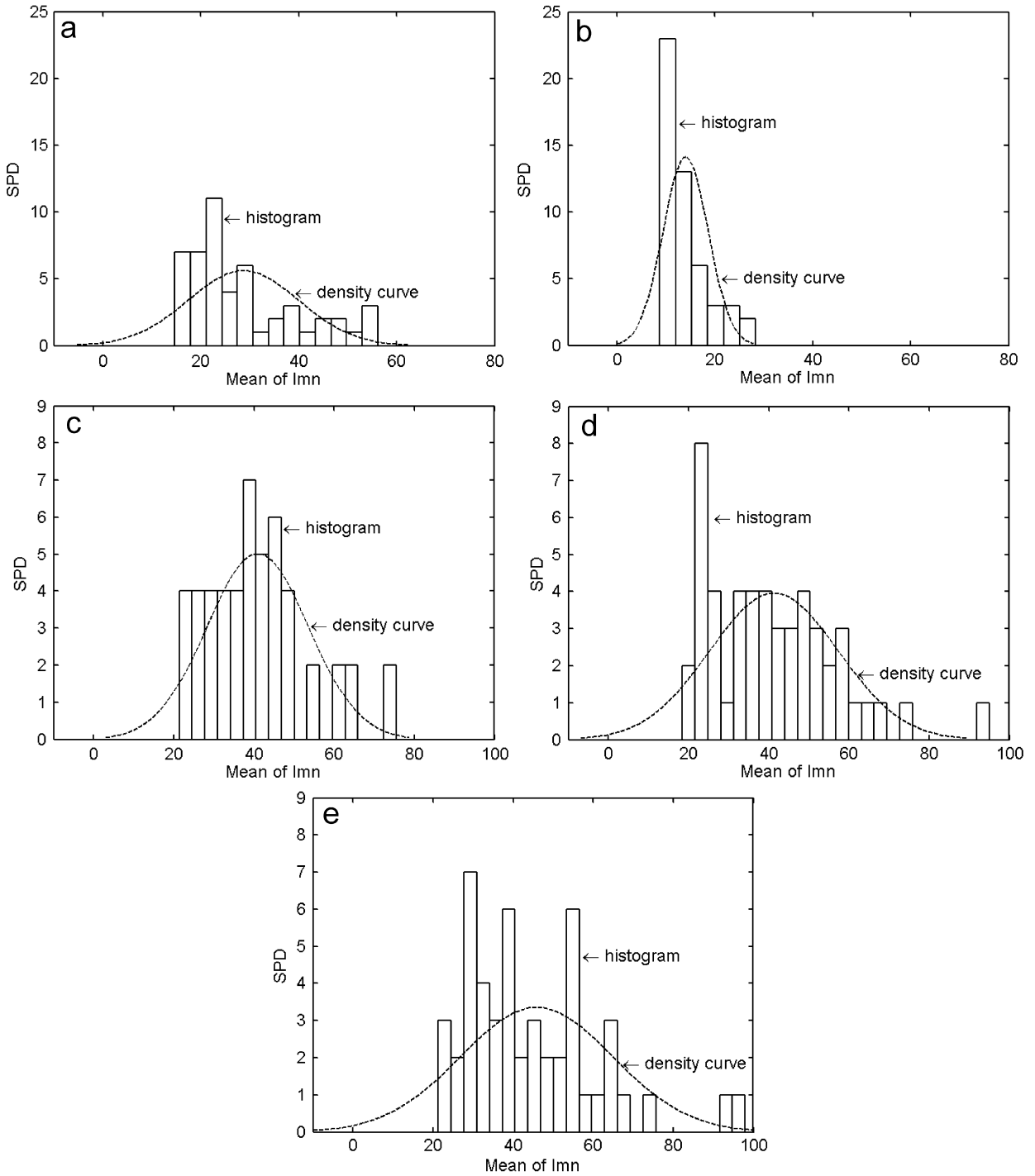

Fig. 13. The statistical probability distribution of the mean of the highest intermittency indices: (a) BLC, (b) BSC, (c) FLC, (d) FSC and (e) NC.

In Fig. 13(d), the mean of SPD was about 40 under FSC condition. The range of SPD was between −8 and 88 under FSC condition, which was larger than that under FLC condition. Fig. 13(e) shows SPD under NC condition. The mean of SPD was about 45 and the range of SPD was between −10 and 100. The mean and

range were larger than the other four conditions. The mean of the highest intermittency indices at the first wavelet scale can be used as feature values to diagnose the different conditions of the water hydraulic motor.

Fig. 14 shows the statistical probability distribution of the variances of the highest intermittency indices at the first wavelet scale under the five piston conditions. Fig. 14(a) shows the mean of the variance SPD was 0.25×10^4 and the range was between -0.5×10^4 and 1×10^4 under FLC condition. Fig. 14(b) shows the mean of the SPD was 0.1×10^4 and the range was between -0.2×10^4 and 0.4×10^4, which were different from that under FLC condition. In Figs. 14(c) and (d), the means under BLC and BSC conditions were 0.425×10^4 and 0.45×10^4. The range of SPD was between -0.4×10^4 and 1.25×10^4 under BLC condition. The range of SPD was between -0.4×10^4 and 1.3×10^4 under BSC condition. Fig. 14(e) shows that the mean was 0.5×10^4 and the range of SPD was between -1×10^4 and 2×10^4. Hence, the means and range of SPD under the five piston conditions were different. The variances of the highest intermittency indices at the first wavelet scale can be used as feature values to diagnose the different conditions of the water hydraulic motor.

The scaling coefficients in the multi-decomposition based on the lifting scheme involve the low frequency of the vibration signals, which is the response of the mechanical structure condition. Fig. 15 shows the statistical probability distribution of the second-order statistical moment of the scaling coefficients at first, second and third scale. Fig. 15(a) shows SPD of the second-order statistical moment of the scaling coefficients at first, second and third scale under BLC condition. The means of SPD at the first, second and third scale were 0.55×10^{-4}, 0.925×10^{-4} and 3×10^{-4}. The ranges of the SPD were between 0.5×10^{-4} and 0.6×10^{-4}, 0.5×10^{-4} and 1.8×10^{-4}, 1×10^{-4} and 5×10^{-4}. Fig. 15(b) shows SPD of the second-order statistical moment of the scaling coefficients at first, second and third scale under BSC condition. The mean of SPD at the first, second and third scale were 0.45×10^{-4}, 1×10^{-4} and 2.2×10^{-4}. The ranges of the SPD were between 0.4×10^{-4} and 0.5×10^{-4}, 0.5×10^{-4} and 1.5×10^{-4}, 0.2×10^{-4} and 4.2×10^{-4}, which were different from that under BLC condition. Fig. 15(c) shows SPD of the second-order statistical moment of the scaling coefficients at first, second and third scale under FLC condition. The mean of SPD at the first, second and third scale were 0.2×10^{-4}, 0.5×10^{-4} and 1.25×10^{-4}, which were less than that under BLC and BSC conditions. The range of the SPD were between 0.1×10^{-4} and 0.3×10^{-4}, 0.3×10^{-4} and 0.7×10^{-4}, 0.7×10^{-4} and 1.8×10^{-4}, which were less than that under BLC and BSC conditions. Fig. 15(d) shows SPD of the second-order statistical moment of the scaling coefficients at first, second and third scale under FSC condition. The mean of SPD at the first, second and third scale were 0.25×10^{-4}, 0.55×10^{-4} and 1.3×10^{-4}, which were less than that under BLC and BSC conditions and different from that under FLC condition. The range of the SPD was between 0.1×10^{-4} and 0.4×10^{-4}, 0.3×10^{-4} and 0.8×10^{-4}, 0.6×10^{-4} and 2×10^{-4}, which were different from that under BLC, BSC and FLC conditions. Fig. 15(e) shows SPD of the second-order statistical moment of the scaling coefficients at first, second and third scale under NC condition. The mean of SPD at the first, second and third scale were 0.25×10^{-4}, 0.5×10^{-4} and 0.95×10^{-4}, which were different from the other four conditions. The range of the SPD was between 0.2×10^{-4} and 0.3×10^{-4}, 0.4×10^{-4} and 0.6×10^{-4}, 0.7×10^{-4} and 1.2×10^{-4}, which were different from the other four conditions. The range and mean of the statistical probability distribution of the scaling coefficients were totally different under different piston conditions.

6.3. Hypothesis testing for SPD to classify the five piston conditions

In order to classify the five piston conditions, the hypothesis testing was applied to compare the SPDs of the values under five piston conditions as shown in Figs. 13–15. Statistical hypothesis testing is the fundamental method used at the data analysis of a comparative experiment. The Kolmogorov–Smirnov (KS)-type test is the commonly used goodness-of-fit tests [26]. The KS test is based on the following test statistic:

$$K = \sup |F^*(x) - S(x)|, \tag{36}$$

where $F^*(x)$ is the hypothesized cumulative distribution function. $S(x)$ is the empirical distribution function based on the sample data. KS statistic is the maximum difference between these functions.

Here the KS test was used to compare the SPD in Figs. 13–15 and shows the differences between the SPDs among the five piston conditions. The null hypothesis for this test is that the two SPDs have the same continuous distribution, that is H_0: $F^*(x) = S(x)$ for all the x from $-\infty$ to ∞. The alternative hypothesis is

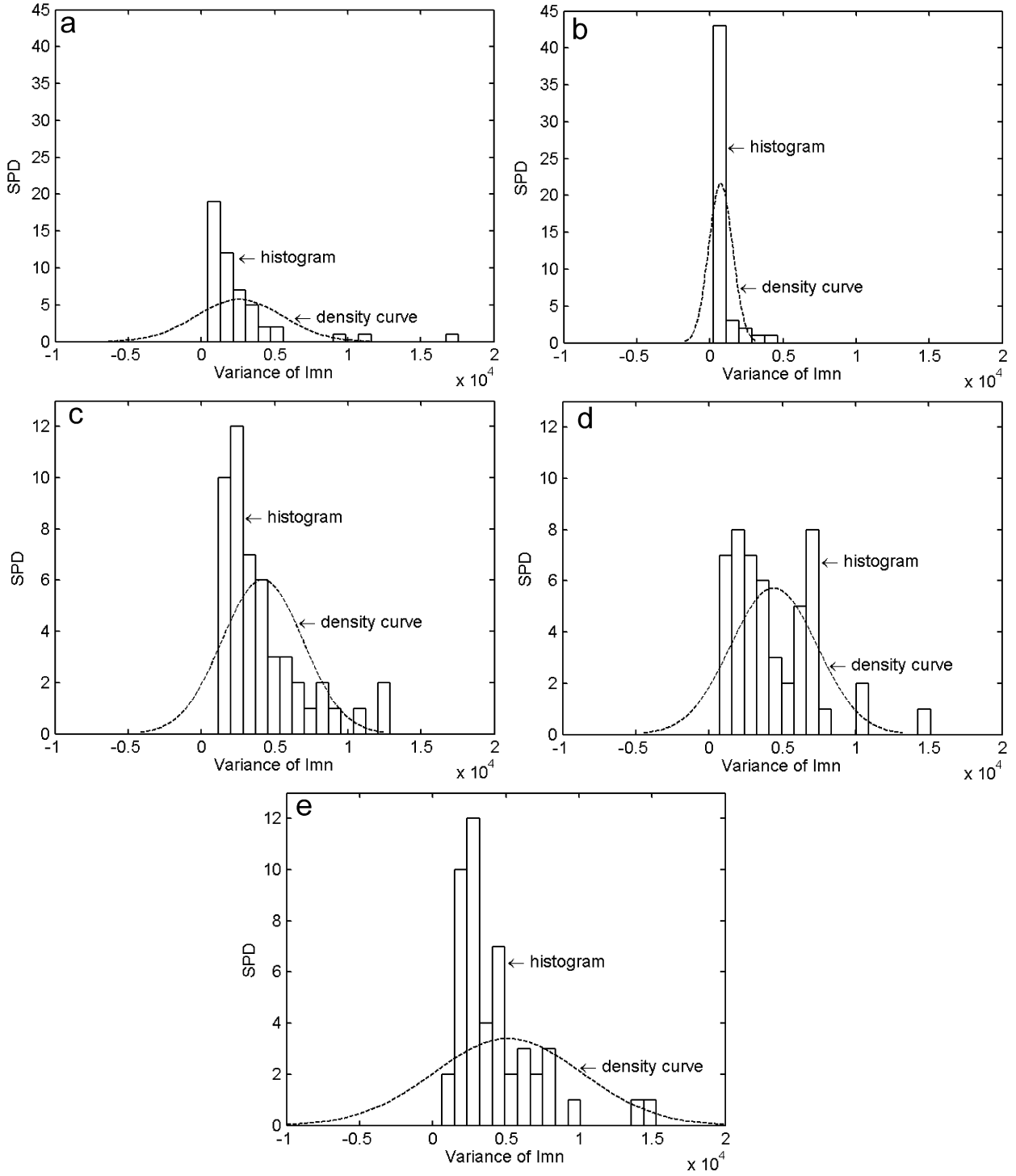

Fig. 14. Statistical probability distribution of the variance of the highest intermittency indices: (a) BLC, (b) BSC, (c) FLC, (d) FSC and (e) NC.

that the two SPDs have different continuous distributions, that is H_1: $F^*(x) \neq S(x)$. The hypothesis that the two SPDs have the same distribution was rejected if the result H is 1. The hypothesis that the two SPDs have the same distribution cannot be rejected if the result H is 0. The p-value represents the statistical significance of the

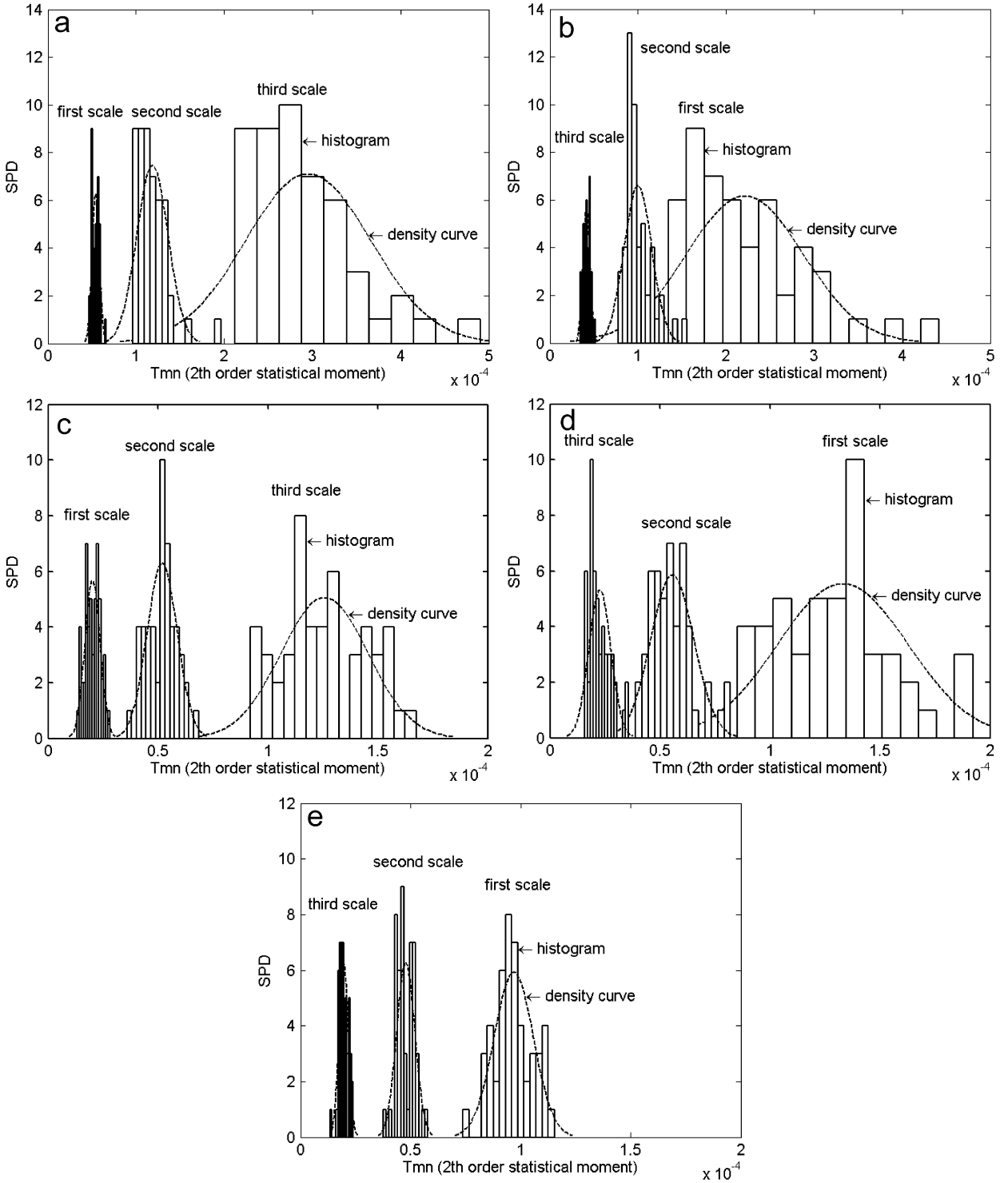

Fig. 15. Statistical probability distribution of the second-order statistical moment of the scaling coefficients at first, second and third scale: (a) BLC, (b) BSC, (c) FLC, (d) FSC and (e) NC.

comparison and confidence level, which is at 5% level. If the p-value is less than 5%, the result H is 1 and H_0 is rejected. The two distributions have the difference. The low p-value rejects the hypothesis H_0. The K-value shows how much difference is between the two SPDs under the piston conditions.

Table 1 shows the results of KS test among the mean SPDs of the highest intermittency indices under the five piston conditions, which is shown in Fig. 13. The values H, p and K among the different piston conditions are shown in Table 1. All the H-values equal to 1 between the BLC and other four piston conditions. The value p is very small and the confidence level is very low. The SPDs of the highest intermittency indices were different under very low confidence level. The H-values between the BSC and the other three conditions were 1. The value p was small and less than 5%. The SPD under BSC condition can be different from the other three conditions. The KS test results among FLC, FSC and NC were unsatisfactory. The values H between FLC and FSC, and NC and FSC were 0 and the values p were more than 5%.

Table 2 indicates the results of KS test among the variance SPDs of the highest intermittency indices, which is shown in Fig. 14. The H-values between the variance SPD of the highest intermittency indices under BLC condition with the other four conditions were 1. The BLC condition was different from other four conditions. The H-values between the BSC and other three conditions were 1. The p-values were small and less than 5%. The SPD under BSC condition can be different from the other three conditions. The results about values of H, p and K among FLC, FSC and NC were not good.

Tables 3–5 show the results of the KS test among the SPD of the second-order statistical moment of the scaling coefficients at first, second and third scale, which were shown in Fig. 15.

In Table 3, all the H-values among the five piston conditions were 1 and the p-values were less than 5% except that between FLC and FSC. The values p between FLC and FSC were 0.2408 and the significance level was 24.08%, which can be used to classify the difference in the SPDs between FLC and FSC condition. The SPD of the second-order statistical moment of the scaling coefficients at first scale can be used to classify the different piston conditions.

Table 4 shows the results of the KS test among the SPD of the second-order statistical moment of the scaling coefficients at second scale. The H-values among the five piston conditions were 1 and the p-values

Table 1
Results of KS test among the mean SPDs of the highest intermittency indices

	BLC	BSC	FLC	FSC	NC
BLC					
H		1	1	1	1
p		2.1318e−14	1.0227e−005	4.2318−004	1.2335−006
K		0.78	0.48	0.4	0.52
BSC					
H	1		1	1	1
p	2.1318e−14		7.2932e−20	3.2843e−18	4.9988e−19
K	0.78		0.92	0.88	0.9
FLC					
H	1	1		0	0
p	1.0227e−005	7.2932e−20		0.5077	0.0951
K	0.48	0.92		0.16	0.24
FSC					
H	1	1	0		0
p	4.2318−004	3.2843e−18	0.5077		0.3584
K	0.4	0.88	0.16		0.18
NC					
H	1	1	0	0	
p	1.2335−006	4.9988e−19	0.0951	0.3584	
K	0.52	0.9	0.24	0.18	

Table 2
Results of KS test among the variance SPDs of the highest intermittency indices

	BLC	BSC	FLC	FSC	NC
BLC					
H		1	1	1	1
p		7.8398e−10	7.1595e−5	4.2318−004	2.7638e−5
K		0.64	0.44	0.4	0.46
BSC					
H	1		1	1	1
p	7.8398e−10		3.2843e−18	1.2488e−16	4.9988e−19
K	0.64		0.88	0.84	0.9
FLC					
H	1	1		0	0
p	7.1595e−5	3.2843e−18		0.6779	0.8409
K	0.44	0.88		0.14	0.12
FSC					
H	1	1	0		0
p	4.2318−004	1.2488e−16	0.6779		0.8409
K	0.4	0.84	0.14		0.12
NC					
H	1	1	0	0	
p	2.7638e−5	4.9988e−19	0.8409	0.8409	
K	0.46	0.9	0.12	0.12	

Table 3
Results of the KS test among the SPDs of the second-order statistical moment of the scaling coefficients at first scale

	BLC	BSC	FLC	FSC	NC
BLC					
H		1	1	1	1
p		1.2561e−7	2.1647e−23	2.1647e−23	6.1544e−23
K		0.56	1	1	1
BSC					
H	1		1	1	1
p	1.2561e−7		1.2488e−16	5.3094e−13	6.1544e−23
K	0.56		0.84	0.74	1
FLC					
H	1	1		0	1
p	2.1647e−23	1.2488e−16		0.2408	1.003e−12
K	1	0.84		0.2	0.7392
FSC					
H	1	1	0		1
p	2.1647e−23	5.3094e−13	0.2408		1.8631e−11
K	1	0.74	0.2		0.7
NC					
H	1	1	0	0	
p	6.1544e−23	6.1544e−23	1.003e−12	1.8631e−11	
K	1	1	0.7392	0.7	

Table 4
Results of the KS test among the SPDs of the second-order statistical moment of the scaling coefficients at second scale

	BLC	BSC	FLC	FSC	NC
BLC					
H		1	1	1	1
p		3.7618e−8	2.1647e−23	2.1647e−23	6.1544e−23
K		0.58	1	1	1
BSC					
H	1		1	1	1
p	3.7618e−8		2.1647e−23	1.3674e−21	6.1544e−23
K	0.58		1	0.96	1
FLC					
H	1	1		0	1
p	2.1647e−23	2.1647e−23		0.0951	1.0198e−4
K	1	1		0.24	0.4367
FSC					
H	1	1	0		1
p	2.1647e−23	1.3674e−21	0.0951		1.7897e−6
K	1	0.96	0.24		0.5183
NC					
H	1	1	1	1	
p	6.1544e−23	6.1544e−23	1.0198e−4	1.7897e−6	
K	1	1	0.4367	0.5183	

Table 5
Results of the KS test among the SPDs of the second-order statistical moment of the scaling coefficients at third scale

	BLC	BSC	FLC	FSC	NC
BLC					
H		1	1	1	1
p		7.2932e−20	2.1647e−23	2.1647e−23	2.1647e−23
K		0.92	1	1	1
BSC					
H	1		1	1	1
p	7.2932e−20		2.1647e−23	1.3674e−21	6.1544e−23
K	0.92		1	0.96	1
FLC					
H	1	1		0	0
p	2.1647e−23	2.1647e−23		0.056	0.1119
K	1	1		0.26	0.2358
FSC					
H	1	1	0		1
p	2.1647e−23	1.3674e−21	0.056		0.0024
K	1	0.96	0.26		0.36
NC					
H	1	1	0	1	
p	2.1647e−23	6.1544e−23	0.1119	0.0024	
K	1	1	0.2358	0.36	

were very small except that between FLC and FSC. The significance level was 24.08%. The SPDs among the five piston conditions were different.

Table 5 shows the same results as that in Tables 3 and 4. All the values H among the five piston conditions were 1 and the values p were very small except that between FLC and FSC. The p-values between FLC and FSC, NC were 0.056 and 0.1119 and the significances were 5.6% and 11.19%, respectively, which can be used to classify the two SPDs between FLC and FSC, NC conditions.

Hence, the SPDs in Figs. 13–15 were statistically different under the piston conditions. They can be used as effective features to classify the piston conditions.

7. Conclusion

In this work, the second-generation wavelet is proposed here as a novel method for the feature extraction from the vibration signals of the water hydraulic motor. The second-generation wavelet consists of a lifting scheme. The algorithm and method of multi-decomposition based on the lifting scheme is developed. The denoise method for the vibration signals is presented on the lifting scheme and the GCV. The relation between SNR and GCV is investigated. The corrupted simulated signal is used to test the proposed denoise algorithm. The multi-decomposition of the vibration signal show the impulse vibration signal clearly. The SPDs of the mean, variance and the second-order statistical moment of the scaling coefficients at first, second and third scale were different and can be used to classify the different piston conditions.

Acknowledgments

The authors wish to thank the School of Mechanical and Aerospace Engineering at the Nanyang Technological University for providing the funding and technical support for this research.

References

[1] G.W. Krutz, Patrick S.K. Chua, *Water Hydraulics—Theory and Applications 2004, Workshop on Water Hydraulics, Proceedings of the Agricultural Equipment Technology Conference (AETC'04)*, Hyatt Louisville, Kentucky, 8–10 February, 2004.
[2] M. Higgins, Water hydraulics—the real World, *Industrial Robot* (23) (1996) 13–18.
[3] C.R. Burrows, Fluid power—progress in a key technology, *International Journal of JSME* 37 (1994) 691–700.
[4] N.D. Manring, The torque on the input shaft of an axial-piston swash-plate type hydrostatic pump, *Journal of Dynamic Systems, Measurement, and Control* (1998) 57–62.
[5] G. Zeiger, A. Akers, Torque on the Swashplate of an axial piston pump, *Transactions of the ASME* (1985) 220–226.
[6] Z.L. Qiu, Z.N. Zhen, Y.Z. Lu, Study on vibrational energy transmission characteristics from cylinder to swashplate within an axial piston pump, *Fluid Power-Proceedings of the Ninth International Symposium*, STI, Oxford, UK, 1990, pp. 261–269.
[7] Z.G. Qi, Y.X. Lu, Vibration source, transmission path response analysis and condition monitoring of hydraulic pumps, *The Journal of Fluid Control* 21 (1) (1991) 61–69.
[8] M.K. Bahr, J. Svoboda, R.B. Bhat, Vibration analysis of constant power regulated swash plate axial piston pumps, *Journal of Sound and Vibration* 259 (5) (2003) 1225–1236.
[9] C.K. Chui, *An Introduction to Wavelets*, Academic Press, Boston, 1992.
[10] A.S. Sekhar, Crack detection through wavelet transform for a run-up rotor, *Journal of Sound and Vibration* 259 (2) (2003) 461–472.
[11] Y. Gao, Q. Zhang, X. Kong, Wavelet-based pressure analysis for hydraulic pump health diagnosis, *Transactions of the ASAE* 46 (4) (2003) 969–976.
[12] J. Iroishi, Y. Li, T. Liang, T. Kurfess, S. Danyluk, Bearing condition diagnostics via vibration and acoustic emission measurements, *Mechanical Systems and Signal Processing* 11 (5) (1997) 693–705.
[13] S.K. Lee, P.R. White, Enhancement of impulsive noise and vibration signals for fault detection in rotating and reciprocating machinery, *Journal of Sound and Vibration* 217 (3) (1998) 485–505.
[14] N. Baydar, A.A. Ball, Comparative study of acoustic and vibration signals in detection of gear failures using Wigner–Ville distribution, *Mechanical Systems and Signal Processing* 15 (6) (2001) 1091–1107.
[15] Z. Chen, C.K. Mechefske, Machine signature identification by analysis of impulse vibration signals, *Journal of Sound and Vibration* 244 (1) (2001) 155–167.
[16] Z. Peng, Y. He, Q. Lu, F. Chu, Feature extraction of the rub-impact rotor system by means of wavelet analysis, *Journal of Sound and Vibration* 259 (4) (2003) 1000–1010.
[17] Danfoss, Inc. 〈http://www.danfoss.com/Nessie/Introduction/index.asp〉, Denmark.

[18] E. Kojima, M. Shinada, Characteristics of fluidborne noise Generated by a fluid power pump, *Bulletin of JSME* 29 (258) (1986) 4147–4155.
[19] K.A. Edge, D.N. Johnston, The secondary source method for the measurement of pump pressure ripple characteristics, *Proceedings of the Institution of Mechanical Engineers* 204 (1990) 33–40.
[20] W. Sweldens, The lifting scheme: a custom-design construction of biorthogonal wavelets, *Applied and Computational Harmonic Analysis* 3 (2) (1996) 186–200.
[21] I. Daubechies, W. Sweldens, Factoring wavelet transforms into lifting steps, *Journal of Fourier Analysis and Application* (1998) 41–44.
[22] D.L. Donoho, I.M. Johnstone, Ideal spatial adaptation via wavelet shrinkage, *Biometrika* 81 (1994) 425–455.
[23] N. Weyrich, G.T. Warhola, De-noising using wavelets and cross validation, *Approximation Theory, Wavelets and Applications* 454 (1995) 523–532.
[24] P. Hall, I. Koch, On the feasibility of cross-validation in image analysis, *Journal of Applied Mathematics* 52 (1) (1992) 292–312.
[25] J. Watton, *Condition Monitoring and Fault Diagnosis in Fluid Power Systems*, Ellis Horwood, Chichester, UK, 1992.
[26] W.J. Conover, *Practical Nonparameteric Statistics*, third ed, Wiley, New York, 1980.